Comparison Between Cross-Track and Conical Scanning Microwave Window Channels Near 90 GHz

August 2000

Prepared by

J. E. WESSEL
Laboratory Operations
Engineering and Technology Group

and

D. J. BOUCHER
DMSP
Space Systems Group

Space Systems Group

20001215 043
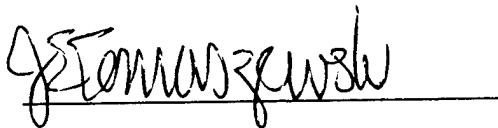
This report was submitted by The Aerospace Corporation, El Segundo, CA 90245-4691, under Contract No. F04701-93-C-0094 with the Space and Missile Systems Center, P. O. Box 92960, Los Angeles, CA 90009-2960. It was reviewed and approved for The Aerospace Corporation by D. J. Gorney, Principal Director. The project officer is Mr. John Tomaszewski.

This report has been reviewed by the Public Affairs Office (PAS) and is releasable to the National Technical Information Service (NTIS). At NTIS, it will be available to the general public, including foreign nationals.

This technical report has been reviewed and is approved for publication. Publication of this report does not constitute Air Force approval of the report's findings or conclusions. It is published only for the exchange and stimulation of ideas.

Mr. John Tomaszewski
Project Officer

REPORT DOCUMENTATION PAGE

Form Approved
OMB No. 0704-0188

1. AGENCY USE ONLY (Leave blank)	2. REPORT DATE August 2000	3. REPORT TYPE AND DATES COVERED

4. TITLE AND SUBTITLE

Comparison Between Cross-Track and Conical Scanning Microwave Window Channels Near 90 GHz

5. FUNDING NUMBERS

F04701-93-C-0094

6. AUTHOR(S)

J. E. Wessel and D. J. Boucher

7. PERFORMING ORGANIZATION NAME(S) AND ADDRESS(ES)

The Aerospace Corporation
2350 El Segundo Boulevard
El Segundo, CA 90245

8. PERFORMING ORGANIZATION REPORT NUMBER

TR-2000(1550)-1

9. SPONSORING/MONITORING AGENCY NAME(S) AND ADDRESS(ES)

Space and Missile Systems Center
Air Force Materiel Command
2430 E. El Segundo Boulevard
Los Angeles Air Force Base, CA 90245

10. SPONSORING/MONITORING AGENCY REPORT NUMBER

SMC-TR-00-37

11. SUPPLEMENTARY NOTES

12a. DISTRIBUTION/AVAILABILITY STATEMENT

Approved for public release; distribution unlimited.

12b. DISTRIBUTION CODE

13. ABSTRACT (Maximum 200 words)

The principal objective of this study was to determine the angular characteristics of the cross-track 92-GHz window channel of the SSM/T-2 microwave water vapor radiometer (T-2) over the ocean surface and to relate measurements from this instrument to corresponding 85-GHz window channel measurements from the conical scanning SSM/I imager. The conical scanner views at constant incidence angle and fixed polarizations, whereas the cross-track instrument scans across incidence angles with changing polarization. A model, based on radiative transfer calculations and Fresnel surface parameterization, successfully interrelated signals from the two radiometers as a function of T-2 scan angle for a significant fraction of the oceanic measurements. This confirmed the angular dependence model and provided a general relationship between 92-GHz SSM/T-2 and 85-GHz SSM/I signals, which is applicable in the absence of depolarization by rain, clouds, or severe sea surface roughness. Intercomparison between instruments, based on surface modeling, may be useful for instrumental calibration, it may assist in evaluation of microwave transmission models, and it does provide a validity test for ocean surface emissivity parameterization and cloud clearing procedures.

14. SUBJECT TERMS

Humidity measurements, microwave radiometry, polarization, remote sensing, satellite applications.

15. NUMBER OF PAGES

11

16. PRICE CODE

17. SECURITY CLASSIFICATION OF REPORT	18. SECURITY CLASSIFICATION OF THIS PAGE	19. SECURITY CLASSIFICATION OF ABSTRACT	20. LIMITATION OF ABSTRACT
Unclassified	Unclassified	Unclassified	

Contents

Figures

Tables

Abstract— The principal objective of this study was to determine the angular characteristics of the cross-track 92-GHz window channel of the SSM/T-2 microwave water vapor radiometer (T-2) over the ocean surface and to relate measurements from this instrument to corresponding 85-GHz window channel measurements from the conical scanning SSM/I imager. The conical scanner views at constant incidence angle and fixed polarizations, whereas the cross-track instrument scans across incidence angles with changing polarization. A model, based on radiative transfer calculations and Fresnel surface parameterization, successfully interrelated signals from the two radiometers as a function of T-2 scan angle for a significant fraction of the oceanic measurements. This confirmed the angular dependence model and provided a general relationship between 92-GHz SSM/T-2 and 85-GHz SSM/I signals, which is applicable in the absence of depolarization by rain, clouds, or severe sea surface roughness. Intercomparison between instruments, based on surface modeling, may be useful for instrumental calibration, it may assist in evaluation of microwave transmission models, and it does provide a validity test for ocean surface emissivity parameterization and cloud clearing procedures.

Index Terms— Humidity measurements, microwave radiometry, polarization, remote sensing, satellite applications.

I. INTRODUCTION

REMOTE sensing satellites typically employ conical or cross-track scanning instruments. The relative merits of these scanners are governed by several factors. Scan angle, response to surface polarization directions, and pixel size are easily held constant in a conical scan, whereas they vary for a simple cross-track scan. Cross-track devices provide views near nadir, where atmospheric path effects are minimized. Measurements from these two types of devices are subject to differing atmospheric paths and the window channels respond differently to surface polarization effects, which were recently studied at 92 and 150 GHz by Felde and Pickle [1]. The other sources of polarization, such as cloud effects and Zeeman-induced polarization from mesospheric oxygen, are expected to be insignificant.

DMSP 5D2 satellites [2]–[6] have both conical and cross-track scanning microwave instruments. This paper compares window channel signals from the 85-GHz conically scanning DMSP SSM/I imager (M/I) with the 92-GHz channel of the cross-track scanning SSM/T-2 water vapor radiometer (T-2).

Pertinent instrumental characteristics are compared in Table I. Both sensors employ heterodyne total-power radiometers. In principle, T-2 calibration is subject to less uncertainty than M/I because the primary scan mirror is always present in the T-2 viewing path, thus, its contributions are removed in the data reduction process. The mirror rotates across the measurement swath and then views a blackbody calibration source, maintained at about 300 K, and finally views deep space (through a short low-loss coaxial feedhorn) for the low temperature calibration. The M/I feedhorn views the primary reflector and is then rotated to directly view a constant temperature blackbody source. A small deflecting mirror intercepts the feedhorn in order to view into cold space. Therefore, M/I calibration is subject to additional uncertainties associated with coupling efficiencies between the mirrors and the feedhorn and possible mirror degradation over the instrument lifetime. The instruments have dissimilar footprints. For T-2 it is about 90 km at nadir for 92 GHz, which greatly exceeds the 15-km footprint of M/I at 85 GHz. The M/I has separate horizontal and vertical polarization channels, whereas T-2 has a single window channel that measures a mixed polarization.

The polarization geometry affecting T-2 is depicted in Fig. 1, with the scanning reflector at an outer scan position.

TABLE I
WINDOW CHANNEL CHARACTERISTICS

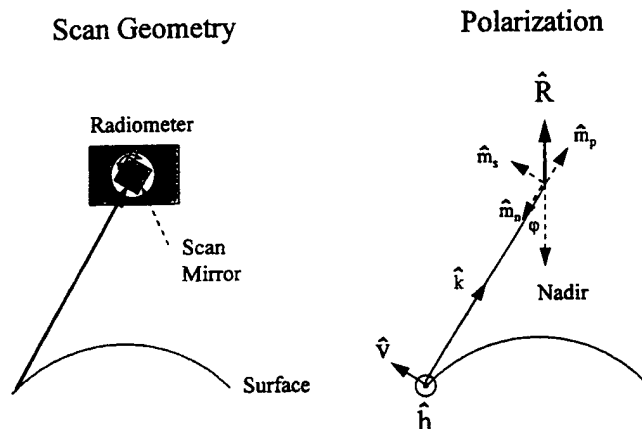|	SSM/I(a)	SSM/T-2(b)
Frequency	85.5 GHz	91.65 GHz
Bandwidth	1.4 GHz	1.5 GHz
Number Pixels in Swath	128	24
Beam Width	1°	6°
Scan Angles (Nadir)	45° Conical	+40.5° to -28.9° Cross-track
NEΔT	1 K	$\leq$0.6 K
Calibration Uncertainty	0.7 K(c)	0.5 K(c)
Polarization	v, h	Mixed and unspecified

Fig. 1. Polarization diagram showing scanning geometry on the left and polarization geometry on the right. The propagation vector is denoted $\hat{k}$, vertical ($\hat{v}$) and horizontal ($\hat{h}$) polarizations are relative to the earth surface. The upwelling radiation is resolved into polarizations ($\hat{s}$) and ($\hat{p}$) by the scan mirror, which is shown rotated by ϕ relative to nadir. Beam propagation is deflected into the plane of the figure by the scan mirror, and the polarization ($\hat{h}$) flips 90° to ($\hat{p}$) at this point. Both ($\hat{s}$) and ($\hat{p}$) are resolved into the principal radiometer polarization $\hat{R}$ and the projections vary as the mirror scans.

Radiation propagates upward to the reflector and is deflected into the radiometer feedhorn, which lies behind the plane of Fig. 1. The metallic reflector is expected to have nearly ideal reflection characteristics [7], based on the surface properties of metals [8], and polarization cross contamination effects should be negligible (polarization cross contamination is used here to denote effects associated with retardation or nonideal reflector geometry, whereas the large effect of polarization mixing upon reflection is treated explicitly). Upwelling radiance polarized in the direction of the surface normal is designated as vertically ($\hat{v}$) polarized. This radiation is polarized perpendicular ($\hat{s}$) to the plane of incidence, which contains both propagation directions and the reflector surface normal. The polarization direction rotates with the mirror scan angle. It projects onto the principal polarization directions of the fixed instrument feedhorn ($\hat{R}$). (In the case of T-2, the vertical feedhorn polarization direction is presumed to be active, although instrument polarization characteristics are undocumented.) The horizontally ($\hat{h}$) polarized surface emission propagates upward with a polarization vector out-of-plane, with respect Fig. 1. The polarization direction of the reflected beam is rotated 90° about the propagation direction, such that it coincides with $\hat{R}$ for $\phi = 0°$. Both ($\hat{v}$) and ($\hat{h}$) components project on the presumed vertical feedhorn polarization at the outer scan angle ($\phi = 40.5°$). Since the field components are uncorrelated, the signal is expected to have an angular dependence given by

$$T_b(\phi) = T_b(\hat{h})\cos^2(\phi) + T_b(\hat{v})\sin^2(\phi) \qquad (1)$$

where ϕ is the nadirial angle and $T_b(\hat{h})$ and $T_b(\hat{v})$ are brightness temperature vectors for purely horizontally and purely vertically polarized radiation. The predicted angle dependence for 92 GHz is illustrated in Fig. 2, which was derived for a mean climatological tropical marine atmosphere (temperature and water vapor for April, 2°S, 180°W [9], [10], 47.5 kg/m² columnar water vapor, and sea surface temperature (SST) from [11] and [12]). The radiative transfer code incorporated
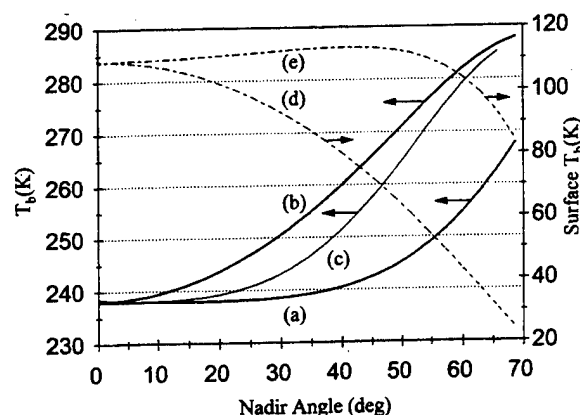

Fig. 2. Theoretical angular dependence of the polarized signals and the surface contribution for a tropical marine environment. The curves represent: (a) $92(\hat{h})$, (b) $92(\hat{v})$, (c) 92 [mixed, according to (1)], (d) the horizontally polarized surface contribution, and (e) the vertically polarized surface contribution.

the 1992 atmospheric transmission model of Liebe et al. [13]–[16]. The heavy solid curves describe pure vertical and pure horizontal polarizations and the mixed signal predicted by (1) is shown as the thin line denoted by (c). Contributions to (a) and (b) from surface blackbody emission plus reflected downwelling emission are indicated by curves (d) and (e). These decrease at large angles, due to increasing atmospheric attenuation.

In the case of a smooth ocean surface, the Fresnel relations [17] provide a convenient estimate for the angular dependence of polarization and were incorporated into the radiative transfer model. The surface-related signal derives from direct blackbody radiance, which is equal to $\varepsilon_s T_s$, where ε_s is the surface emissivity and T_s is the surface temperature. Surface emissivity is equal to $(1 - R)$, where the reflectivity (R) depends on angle of incidence and polarization. R also determines the amount of downwelling atmospheric radiance reflected into the upward path. R was calculated from dielectric properties of water, which were modeled from recent measurements at 89 GHz reported by Ellison et al. [18], [19]. The data were fit to a double dispersion model, as suggested in Liebe et al. [20]. Salinity was assumed to be 30%; however, for the purposes of this investigation, dielectric properties at and above 85 GHz are not sensitive to salinity [18]. Reflectivities and emissivities estimated from the new data differed substantially, for regions with sea surface temperature (SST) below about 283 K, from those suggested by Liebe et al. and by Klein and Swift [21], resulting in generally improved correspondence between models and data.

Fig. 3 presents a comparison between a histogram of SSM/I measurements at 85 GHz (vertically polarized) for a number of passes over the central Pacific Ocean with a forward calculation performed by using the April tropical marine atmosphere with 47.5-kg/m² water vapor [9]–[12] and the SST's reported for the measurement period from the Central Equatorial Pacific Experiment (CEPEX). The average brightness temperature measured for data screened for clouds, rain, and surface roughness was 274.2 K, with a 2.0-K standard deviation versus the calculated 271.7 K. (Screening rejected data with $T_b(85v) - T_b(85h) < 15$ K.) Climatology provides
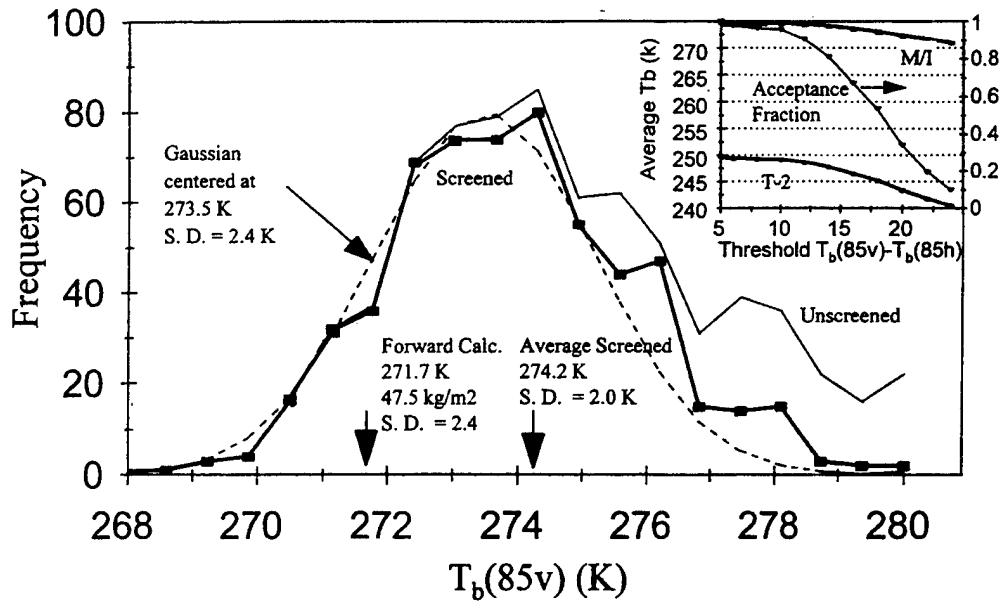
4

Fig. 3. Histogram of SSM/I $T_b(85v)$ from five orbital passes over the central Pacific from 7°S to 3°N in March 1995. The upper right insert shows the influence of screening threshold on the averages for M/I $T_b(85v)$ and T-2 $T_b(92)$, with corresponding data acceptance rates.

an estimate of ±10% rms variability for the columnar water, and the forward calculation predicts that this corresponds to a 2.4-K standard deviation in $T_b(85v)$. The dashed line in Fig. 3 corresponds to a Gaussian with this width. It is adjusted to match the low-temperature side of the measurement histogram. The center of this distribution occurs at 273.5 K, which is 1.8-K above the calculated value. The rationale for using the Gaussian centroid to estimate the clear weather smooth surface average brightness temperature is that surface and cloud conditions skew measurements to higher temperatures (shown by the thin solid line in Fig. 3, which is the full unscreened data set). Modest screening has no effect on the low brightness temperature data (none of the pixels with $T_b(85v) < 272.5$ K are rejected with a screening threshold of 15 K) and the Gaussian provides an ideal fit to the lower half of the distribution. The 1.8-K discrepancy between the Gaussian centroid and the forward calculation can be removed by increasing the water vapor column 9% relative to climatology, or by correspondingly adjusting the water vapor continuum coefficient in the radiative transfer model.

Radiative transfer calculations were used to compare window channel signals for the two sensors. Fig. 4 models the angle dependence of the ratio between the T-2 and M/I signals for equatorial oceanic scenes, as a function of scan angle (ϕ), for various amounts of columnar water vapor. The ratio R is given by

$$R = [T_b(92, \phi', \hat{h})\cos^2(\phi) + T_b(92, \phi', \hat{v})\sin^2(\phi)]$$
$$/[T_b(85, 53°, \hat{h})\cos^2(\phi) + T_b(85, 53°, \hat{v})\sin^2(\phi)] \quad (2)$$

where ϕ' is the earth incidence angle ($\phi' = 53°$ for M/I).

II. DATA ANALYSIS

Data sets obtained over cloud-free regions in the tropical Pacific Ocean were examined in order to compare collocated
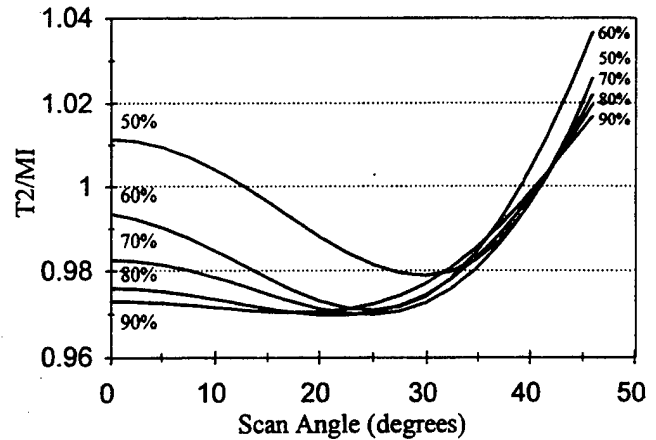
Fig. 4. Predicted angular dependence of R, the ratio between the 92-GHz SSM/T-2 signal and the correspondingly adjusted 85-GHz SSM/I signal, as a function of angular viewing positions for equatorial atmospheres with various nominal relative humidities (75% RH corresponds to the climatological average).

signals from the T-2 and M/I instruments and to evaluate the angular dependence of T-2. The M/I measurements, which are made at a constant scan angle and with two polarizations, provided the reference needed to account for variations in polarization and incidence angle that occur across the T-2 scan. The solid line in Fig. 5 passes through T-2 data points measured in a relatively cloud-free equatorial region. The horizontal axis represents angular displacement from nadir at the 24 discrete measurement positions. A number of pixels are shown for each position, corresponding to successive scans across the ascending track.

Open circles represent the collocated M/I pixels, which have been adjusted for T-2 polarization mixing (1) and multiplied by the factor R (2) in order to compensate for atmospheric path differences. R was optimized specifically for this data set by adjusting columnar water vapor such that the rms variance

5

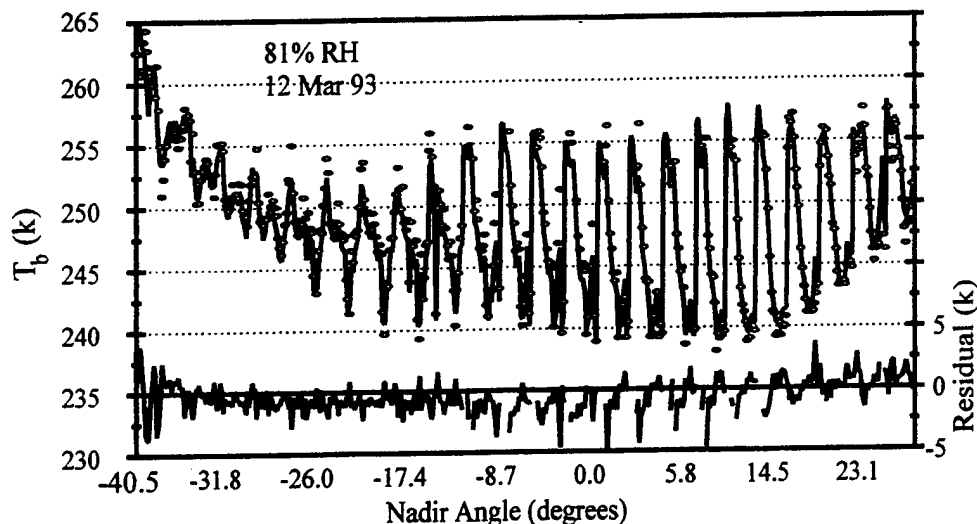Fig. 5. Angle dependence of data for a cloud-free region of the tropical Pacific (7°S to 3°N, 190°E to 203°E, March 12, 1993). The solid line connects SSM/T-2 measurements at 92 GHz and the open circles represent the corresponding adjusted 85-GHz M/I signals. SSM/I measurements.

TABLE II
T-2 COMPARED WITH M/I WINDOW CHANNEL DATA

Data Set	σ(K)	Bias (K)[a] T2-M/I	Water[b] (kg/m²)	T2 Pixels Used	T2 Pixels[c] Excluded	Region	Selected
12 Mar 93	1.23	-0.47	56 (2.0)	433	45	7S-3N	190-203E
f11-17216	1.46	0.16	59 (1.2)	159	55	2S-2N	249-260E	30 Mar 95, 65S-10N
f11-17211	1.48	-0.58	56 (2.3)	171	24	2S-2N	208-217E	30 Mar 95, 45S-45N
f11-17218	1.25	-0.29	58 (1.4)	81	39	2S-2N	223-235E	31 Mar 95, 55S-55N
f11-17204	1.47	-0.18	59 (2.2)	155	111	0-5N	222-235E	30 Mar 95 20N-59N
Average[d]	1.38	-0.3	58				
Uncertainty		0.3[d]	3.2[d]				

(a) Bias evaluated from full scans.

(b) Columnar water giving the best RMS fit between M/I data and the observed T-2 $T_b(92)$, with statistical errors in parentheses.

(c) Exclusion criterion: $T_b(85v) - T_b(85h) < 15$ K.

(d) Uncertainty estimated using Student's t-test with a 90% level of confidence: (S/5)*t₀.₄ where S is sample standard deviation

between the T-2 and corrected M/I data was minimized. The difference between the T-2 measurements and the corrected M/I values are shown by the residuals, plotted at the bottom of the Fig. 1. Data were screened for contamination by clouds and surface roughness by rejecting all pixels with $T_b(85v) - T_b(85h) < 15$ K. The criterion was derived from forward calculations that predict a difference of 17 K for 60-kg/m² columnar water vapor with a tropical temperature profile. The difference increases with decreasing water vapor. Differences smaller than 15 K are strongly indicative of heavy cloud cover, precipitation, or highly rough or foam-covered ocean surfaces.

Similar comparisons were performed for four other tropical data sets. These were of smaller size and were originally acquired for study of storm fronts; therefore, data rejection was relatively high in regions of storm activity, as shown in Table II. R was separately optimized for each cleared data set (by adjusting the water vapor column); however, the effects of optimization and clearing were both weak (rms increased 0.3 K when the water vapor column was decreased from 60 to 33 kg/m²).

Further confirmation of the ability to model angle dependence was obtained by examining extensive data sets covering
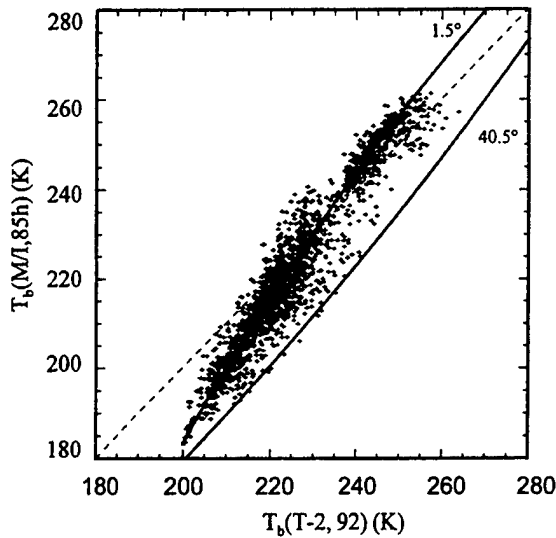
6

Fig. 6. Scatter plot of raw SSM/I 85($\hat{h}$) measurements versus the collocated 92-GHz SSM/T-2 measurements, for orbital passes f11-17211 (45°S to 45°N) spanning the central Pacific Ocean. All SSM/T-2 scan angles are represented. The data were not cloud-cleared and include an extensive frontal system. The upper solid curve, labeled 1.5°, summarizes the results for $\phi = 1.5°$ from model calculations for a variety of atmospheres. Corresponding results for the outer scan position $\phi = 40.5°$ fall along the lower solid line.

oceans from 65°S to 55°N. This analysis did not require adjustment of the M/I data. Fig. 6 intercompares T_bs for collocated M/I and T-2 window channels for three ascending orbital tracks over the south Pacific Ocean. The vertical axis represents the M/I $T_b(h)$ measurements at $\phi = 45°$, and the horizontal axis includes the T-2 data for all incidence angles. The measurements are quite different for the two sensors. For unpolarized emission and ideal angle independent instruments, the data would lie along a line of near unit slope. The actual data cluster below the unit slope line for low temperatures and tend to cross over the line near 225 K. At high temperatures, the data asymptotically approach a vertically displaced line of unit slope.

Modeling was applied to a variety of atmospheres in order to interpret the scatter plots. The 92-GHz T_b was calculated at $\phi = 1.5°$ and 40.5°, corresponding to the range of scanned nadirial angles for the variety of measured and simulated atmospheres encountered along the satellite ground track (representative oceanic profiles including eight climatological estimates [9]–[12], [22], 15 measurements from CEPEX and CASP experiments, and six coastal profiles from the NCDC sounding database [23] with SST's from the Oort database [11]). Calculations were repeated for M/I($\phi = 45°$). The M/I T_bs were plotted against the calculated T-2 T_bs and the results were used to derive the smooth solid curves shown in Fig. 6, defining the upper and lower bounds expected for the T-2 T_bs, as the beam scans from 1.5 to 40.5°. The bounding curve for $\phi = 40.5°$ is well described by a linear function, and a quadratic function is required to fit the 1.5° results. Rms errors between the forward calculations and the model curves were 0.7 and 0.47 K, respectively. The boundary for $\phi = 40.5°$ lies exclusively below the unit slope line, implying that the M/I measurements (for clear weather over smooth oceans) should

be lower than the corresponding T-2 measurements at the outer scan positions.

M/I measurements are predicted to fall below the $\phi = 1.5°$ T-2 measurements for low-temperature atmospheres. An inversion is predicted to occur above 230 K, where the M/I measurements are expected to exceed the corresponding $\phi = 1.5°$ T-2 measurements. The real data include extensive cloud systems with highly scattering precipitation cells and areas with rough ocean surfaces. Both effects tend to reduce surface polarization and displace data from the predicted anisotropic behavior. Small, intensely scattering rain cells would tend to increase T_bs for scattered M/I pixels, relative to the larger regions viewed by T-2. Another factor that may contribute to the spread in Figs. 5 and 6 is atmospheric inhomogeneity, which is sensed differently by the two instruments. Differing response to surface and cloud inhomogeneity is also a likely source of noise.

Additional confirmation of the above model was provided by stratifying the data in terms of viewing angle and rejecting data originating from intensely scattering frontal regions. The data in these subsets is shown in Fig. 7, corresponding to T-2 $\phi = 1.5$–40.5°. The model curves in Fig. 7 are adjusted for the T-2 viewing angles. It is immediately apparent that the stratified data follow the trends predicted by the theoretical model and that the anticipated spread is reduced to a narrow range. The standard deviations of data points relative to the model range from about 2 to 4 K.

The frontal system responsible for the highly scattered data is shown in Fig. 8(a). This is a 92-GHz image of the front, which is centered to the east of Japan. Fig. 8(b) plots the absolute values of the error, calculated as the difference between the 85-GHz T_bs and the model function. Large deviations are concentrated near the intense front and a few occur in more isolated regions. The higher resolution M/I image reveals small precipitation or cloud cells near the pixels that have large deviations. Fig. 8(c) shows a M/I polarization mapping obtained from $T_b(\text{M/I } 85h) - T_b(\text{M/I } 85v)$. This confirms that the frontal regions are highly depolarized, a situation in which the polarization model does not apply. It is noteworthy that large deviations do not occur uniformly throughout the depolarized regions. The polarization diagnostic was explored for use in screening data. It was readily possible to reduce rms between screened data and the model to less than 2 K by applying a strict polarization anisotropy requirement, however, the corresponding rate of data rejection was 90%. A more useful screening requirement was identified:

$$T_b(\text{M/I } 85v) - T_b(\text{M/I } 85h) > 15. + 0.6 \times \text{abs(Latitude)} \text{ (K)}. \tag{3}$$

It accounts for the general increase in polarization with latitude that is due to decreasing water vapor attenuation. Data from a number of orbital tracks conformed to the range of rms deviations represented in Fig. 7 (2–4 K) when screened by this criterion. The average rejection rate was 62% for the five data sets covering 65 S to 60 N in the mid-Pacific Ocean. (Note that this is larger than the 22% rate for the tropical regions of Table II.)
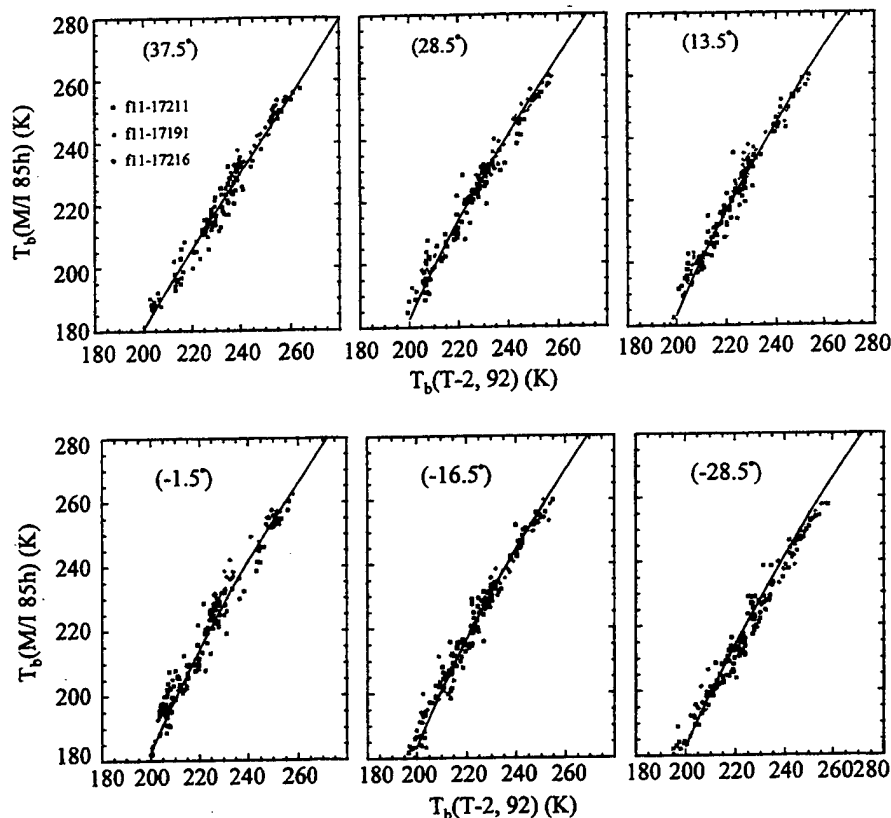
7

Fig. 7. Angle resolved scatter plots for three orbital tracks from 55°S to 55°N across the central Pacific Ocean (fl1-17211, fl1-17216, and fl1-17218). The solid line is the model prediction for the designated viewing angle. Scan angles are indicated in the graphs. Data were screened for wind and clouds by requiring that $T_b(85v) - T_b(85h) > 15. + 0.6^*$ absolute (latitude) (K). More stringent screening greatly reduced variance relative to the model, however, data rejection increased rapidly.

Rudimentary considerations were applied in order to estimate the influence of sea surface roughness on the spread of data. The two-scale wind-induced roughness calculations by Guillou et al. [24], [25] (for 89 GHz and wind velocity of 7 m/s) were compared to brightness temperatures calculated for smooth water surfaces. The results indicate that the wind induced changes in the T-2 signals at 40.5° nadir angle and 7 m/s are about +11 K, at 20° about +16 K, and at 0° about +17 K. The corresponding shifts for M/I are about +25 K in the horizontal channel and −11 K in the vertical channel. This implies that wind-induced shifts reflected in the data of Fig. 7 lie roughly along the direction of the predicted curves relating M/I signals to T-2 signals.

III. DISCUSSION

The T-2 and adjusted M/I data shown in Fig. 5 are in excellent agreement. The rms deviation between collocated measurements is 1.3 K. This is small considering that the atmosphere is not uniform as is assumed in the adjustment model. The effects of atmospheric variation can be discerned across the scans in that the quality of fit between T-2 and M/I data can be improved in localized regions by choosing Rs that are optimized for different amounts of water vapor. It is not clear why it is necessary to increase atmospheric moisture above climatological averages in order to achieve best fit to the equatorial data. A 9% increase with respect to climatology brings forward calculations for $T_b(85v)$ into agreement with

equatorial measurements. A larger increase is required for optimal prediction of T-2 angular dependence. The trend is consistent with prior suggestion [26] for upward revision of the water vapor continuum coefficient, however, it is unclear why the angle dependent estimate and direct forward calculations provide significantly different estimates. One possibility is that the Gaussian centroid method used to estimate $T_b(85v)$ excludes valid high temperature data, biasing the estimated average $T_b(85v)$ low, as shown in the threshold dependence insert in Fig. 3. Normal incidence T-2 measurements are more sensitive to the threshold than M/I, therefore, anomalously high moisture would be required to compensate for the bias. Another possibility is that the revised surface and atmospheric attenuation models are inaccurate. The parameterization of emissivity data employed in this work is subject to an error of about ±0.004 emissivity at 85.5 GHz in the range 285–303 K. The corresponding brightness temperature errors are much less than 1 K for equatorial regions.

Fig. 4 indicates that the spread in R as a function of columnar water is minimized above 30°, which occurs because the atmospheric path for the T-2 begins to approach that for the M/I. This suggests that high angle measurements are most appropriate for deriving interinstrument calibrations. This effect was readily observed when the data were analyzed for various assumed average columnar densities. The outer portions of the curves did not change substantially when water vapor varied from 40–60 kg/m^2, whereas the low
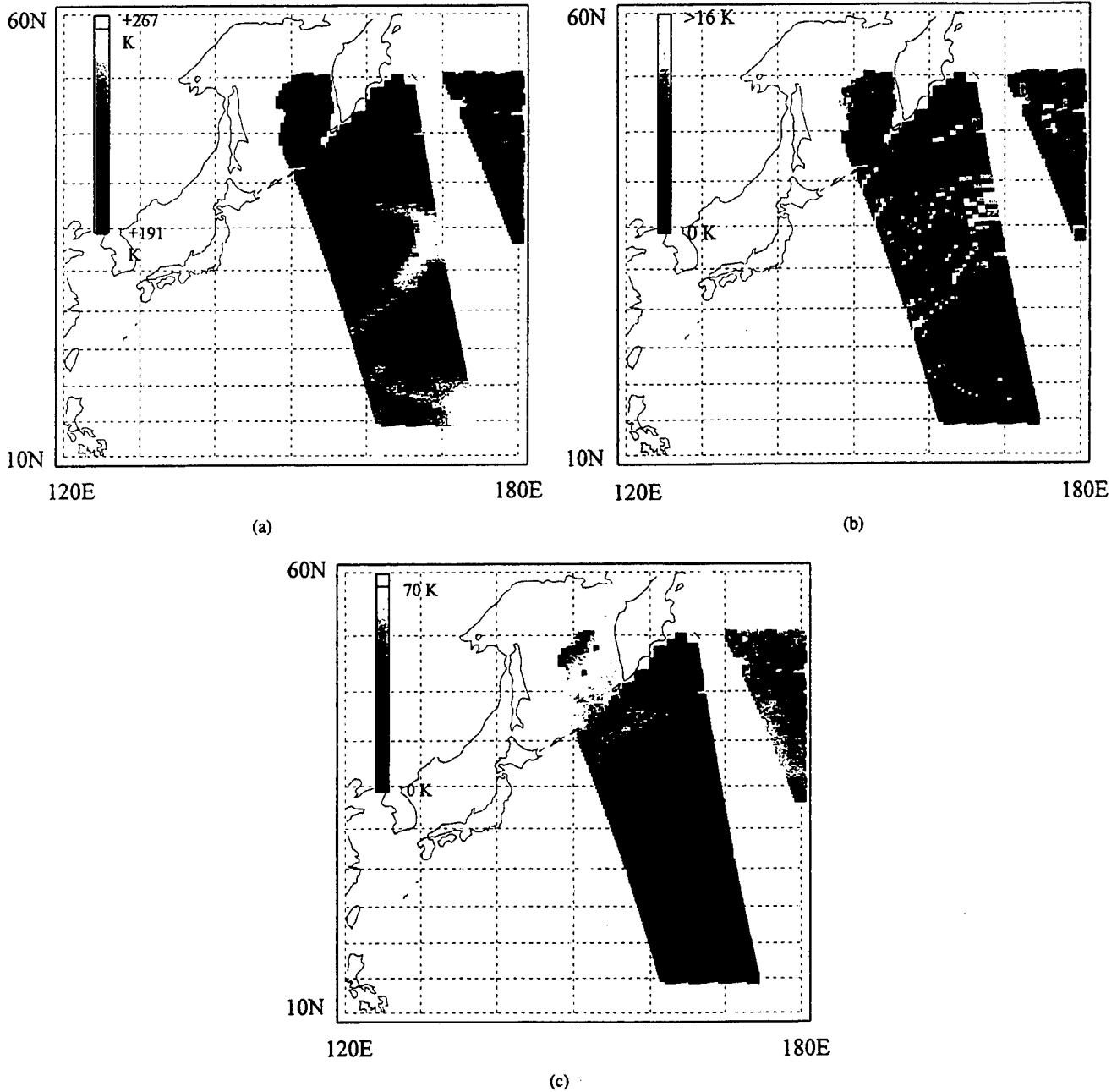
8

(a)

(b)

(c)

Fig. 8. A frontal system to the east of Japan imaged in the 92-GHz SSM/T-2 window channel. (a) The brightness temperature map. (b) The error map obtained from the absolute difference between the model SSM/I brightness temperature (calculated from the observed SSM/T-2 T_b) and the observed SSM/I brightness temperature. (c) A map of polarization anisotropy generated from the difference SSM/I $T_b(85h) - T_b(85v)$. High anisotropy is represented by lighter shading.

angle portions of the curve changed substantially. However, interinstrument bias (Table II) calculated for scan angles >30° was within 0.1 K of that obtained by considering all data and optimizing R for the full scan. Therefore, it is concluded that the uncertainties associated with varying atmospheres are relatively small when averaged over typical scans. Restricting data to angles greater than 30° has the adverse effect of increasing statistical error.

The second method of analysis (scatter plots of M/I $T_b s$ versus T-2 $T_b s$) avoids the need for the adjustment procedure. The curves in Fig. 7 demonstrate the predicted angular dependence over a variety of climatic conditions, accounting for 99.2% of the variance between the measured and predicted

T_b(M/I, h). The relationship between M/I and T-2 $T_b s$ is linear at large angles and nonlinear near nadir [Fig. 7(a)]. In contrast, T-2 $T_b s$ increase nonlinearly with angle at large scan angles, as shown in Figs. 2 and 4, causing the density of data points to decrease toward the 40.5° model curve in Fig. 6.

The spread of data points in Fig. 7 (RMS ~ 3 K, relative to the predicted curves) may be associated with instrumental noise, changes induced by surface roughness, residual uncleared precipitation, clouds, and variations with respect to the model atmospheres. The total random instrumental noise is expected to be less than 1.6 K, based on noise characteristics of the M/I and T-2 instruments. Bias errors were estimated from the difference between the average calculated

9

T_b and the estimated T_b based on the corresponding T-2 measurements for each scene station and each satellite pass. Significant bias, relative to the uncertainty in mean values, was observed for views near nadir, with an average bias of about 0.6 ± 0.1 K for -13.5 to $+16.5°$. The bias arises from errors in model parameterization (estimated to be ≤ 0.5 K) combined with instrumental bias (unknown). Uncertainty in the mean increased at large scan angles, and as a result, it is not possible to verify the significance of the apparent changes in average bias near the edge of scan. Correlation of bias as a function of scan angle was examined for five orbital passes. The correlation coefficients ranged from 0.8 to -0.6, with an average for the off-diagonal correlation of 0.09. This implies that scene station dependence is statistically insignificant. The quality of the model function was tested by comparing the correlation coefficients between data and model curves with those calculated between the data and an arbitrary cubic equation that was optimally fit by least squares. In both cases the correlation coefficients were about 0.992 (data points exceeding four standard deviations relative to model curves were excluded), implying that the model functional form is reasonably optimized.

The most notable deviations occur for data points lying outside the region predicted by the model (which is to the left of the 1.5° curve in Fig. 6 and is characterized by values of $T_b(M/I) - T_b(T-2)$ that are inconsistent with the polarization model or with isotropic scattering, assuming both sensors have identical fields of view). A detailed analysis of these points in six satellite tracks indicates that they arise from small intensely scattering frontal cells that subtend a significant fraction of the small M/I footprint, but are less significant in the larger T-2 footprint. The highly nonuniform pattern of deviations in the error map [Fig. 8(b)] probably occurs because the error depends on agreement between the T-2 based model predictions and the M/I measurements, which do not represent exactly coincident views. In contrast, the polarization map [Fig. 8(c)] is smooth, even within highly depolarizing frontal regions, because the polarization is derived from precisely collocated M/I 85(h) and 85(v) pixels.

Modeling for effects of wind-induced surface roughness is generally consistent with observations. Although winds are expected to cause major changes in the brightness temperatures for the two instruments, the M/I horizontal polarization channel is predicted to change in the same direction as T-2. Although the magnitudes of the changes are different, the ratios are such that the relative changes generally occur along the direction defined by the theoretical relationship between M/I and T-2 signals. Essentially all the spread observed in the cloud-cleared data of Fig. 7 is consistent with anticipated wind-induced roughness.

Finally, the accuracy of the boundary curves depends on the validity of the forward calculations. The calculations are subject to uncertainty in the water vapor continuum contribution, however, this is a small effect in terms of the Fig. 7 model curves. Low temperature regions are most susceptible to surface parameterization error as a consequence of high atmospheric transmission. The surface emission contributions calculated on the basis of the Ellison *et al.* measurements is consistent with the data, whereas corresponding contributions calculated using the Liebe *et al.* parameterization are up to 6 K higher than observed at low temperatures. Model differences are small in the range 283–303 K.

IV. CONCLUSION

In summary, comparison between the collocated data and the radiative transfer model clearly establishes that the polarization of the T-2 92-GHz channel rotates with scan angle in accordance with ideal reflection from a tilting mirror. The difference signals between the 92-GHz T-2 and 85-GHz M/I window channels are relatively insensitive to atmospheric variation over tropical oceanic regions. Based on this observation the interinstrument calibration bias is estimated to be -0.3 (± 0.3) K [T-2(92) $-$ M/I(85v)]. The success in interrelating signals between conical and cross-track scanners suggests that it should be possible to retrieve essentially equivalent window channel information, given polarization data from both types of instruments, over clear oceanic regions.

In the future, it may be possible to use the intercomparison measurements to validate instrument calibration and to test atmospheric transmission models. The existing data suggest that the calibration error between M/I at 85 GHz and T-2 at 92 GHz is less than that implied by the instrument performance specifications. The analysis implies that further attention should be given to evaluating the water vapor continuum coefficient in atmospheric transmission models. A firm recommendation is not warranted due to uncertainty in climatological sampling, uncertainty in the influence of screening threshold, and inadequacy of modeling for surface wind effects. These issues will be addressed in future work.

The data analysis indicates that a Fresnel surface model applies to a significant fraction of cloud-free 90-GHz oceanic measurements. M/I polarization information provides a useful acceptance criterion. This suggests that it may be appropriate to include a surface model in physical retrievals that use T-1, T-2, and M/I oceanic observations, provided an algorithm is used to flag data contaminated by rain, clouds, or rough surface conditions.

REFERENCES

[1] G. W. Felde and J. D. Pickle, "Retrieval of 91 and 150 GHz Earth surface emissivities," *J. Geophys. Res.*, vol. 100, no. D10, pp. 20855–20866, Oct. 1995.

[2] W. Kreiss, A. Strogryn, G. Poe, D. Kieu, and R. Dickey, "Atmospheric propagation and remote sensing III," in *Proc. SPIE*, vol. 2222, pp. 34–54, Apr. 1994.

[3] D. J. Boucher, B. H. Thomas, and A. M. Kishi, "Performance of the DMSP SSM/T-2 microwave radiometer: A comparison between sensor derived, model analyzed, and radiosonde measured moisture variables," in *Proc. 73rd Annu. Mtg., Amer. Meteorol. Soc.,* Anaheim, CA, Jan. 1993, pp. J150–J152.

[4] V. J. Falcone *et al.,* "SSM/T-2 calibration and validation data analysis," Phillips Laboratory, Hanscom AFB, MA, Tech. Rep. 92-2293, Nov. 1992.

[5] N. C. Grody, "Remote sensing of the atmosphere from satellites using microwave radiometry," in *Atmospheric Remote Sensing by Microwave Radiometry,* M. A. Janssen, Ed. New York: Wiley, 1993, ch. 6.

[6] J. Hollinger, "DMSP special sensor microwave/imager calibration/validation final report," Naval Res. Lab., Washington, DC, vol. 1, July 1989.

[7] D. Corson and P. Lorrain, *Introduction to Electromagnetic Fields and Waves.* San Francisco, CA: W. H. Freeman, 1962, ch. 11, pp. 385–396.

[8] A. Zangwill, *Physics at Surfaces.* Cambridge: Cambridge Univ. Press, 1988, ch. 11, pp. 163–182.

[9] A. H. Oort, "Global atmospheric circulation statistics, 1958–1973," NOAA Professional Paper no. 14, Washington, DC: U.S. Government Printing Office, 1983.

[10] _____, OASIS, "Mean air temperature," http://ingrid.ldgo.columbia.edu/SOURCES/.OORT /.Mean/.tair.

[11] _____, "Sea surface temperature," http://ingrid.ldgo.columbia.edu/SOURCES/.OORT/.Mean/.SST.

[12] J. P. Peixoto and A. H. Oort, *Physics of Climate.* New York: Amer. Inst. Phys., 1992, ch. 12, pp. 270–307.

[13] H. J. Liebe and D. H. Layton, "Millimeter-wave properties of the atmosphere: Laboratory studies and propagation modeling," Boulder, CO, NTIA Rep. 87-224, Oct. 1987.

[14] H. J. Liebe, "An updated model for millimeter wave propagation in moist air," *Radio Sci.,* vol. 20, no. 5, pp. 1069–1089, Sept./Oct. 1985.

[15] _____, "MPM—An atmospheric millimeter wave propagation model," *Int. J. Infrared Millimeter Waves,* vol. 10, no. 6, pp. 631–650, June 1989.

[16] H. J. Liebe, P. W. Rosenkranz, and G. A. Hufford, "Atmospheric 60-GHz oxygen spectrum: New laboratory measurements and line parameters," *J. Quant. Spectrosc. Radiat. Transfer,* vol. 48, nos. 5/6, pp. 629–643, Nov. 1992.

[17] M. Born and E. Wolf, *Principles of Optics.* Oxford: Pergamon, 1970, ch. 15.

[18] C. Guillou, L. Eymard, W. Ellison, K. Lamkaouchi, G. Delbos, and C. Prigent, "New permitivity measurements and interpolation functions for natural sea water," in *Proc. 5th Specialist Mtg. Microwave Radiometry Remote Sensing Environment,* Boston, MA, Nov. 1996, paper E6.

[19] W. Ellison *et al.,* "New permitivity measurements and interpolation functions for natural sea water," *Radio Sci.,* submitted for publication.

[20] H. J. Liebe, G. A. Hufford, and T. Manabe, "A model for the complex permitivity of water at frequencies below 1 THz," *Int. J. Infrared Millimeter Waves,* vol. 12, no. 7, pp. 659–675, July 1991.

[21] L. A. Klein and C. T. Swift, "An improved model for the dielectric constant of sea water at microwave frequencies," *IEEE Trans. Antennas Propagat.,* vol. AP-25, pp. 104–111, Jan. 1977.

[22] V. E. Zuev and V. S Komarov, *Statistical Models of the Temperature and Gaseous Components of the Atmosphere.* Dordrecht, The Netherlands: D. Reidel, 1987.

[23] NCDC, "Science-quality real time upper air," extracted from NCDC archive at http://hurricane.ncdc.noaa.gov/ cgi-bin/codiac/dss2.59.

[24] C. Guillou, C. Prigent, S. English, and D. Jones, "Sea surface emissivity models at millimeter waves: Validation from aircraft measurements at 89 and 157 GHz," in *Proc. Int. Conf. Geosci. Remote Sensing,* Tokyo, Japan, Aug. 1993.

[25] A. Guissard and P. Sobieski, "An approximate model for the microwave brightness temperature of the sea," *Int. J. Remote Sensing,* vol. 8, no. 11, pp. 1607–1627, Nov. 1987.

[26] S. J. English, C. Guillou, C. Prigent, and D. C. Jones, "Aircraft measurements of water vapor continuum absorption at millimeter wavelengths," *Q. J. Roy. Meteorol. Soc.,* vol. 120, no. 517, pp. 603–625, Apr. 1994.

LABORATORY OPERATIONS

The Aerospace Corporation functions as an "architect-engineer" for national security programs, specializing in advanced military space systems. The Corporation's Laboratory Operations supports the effective and timely development and operation of national security systems through scientific research and the application of advanced technology. Vital to the success of the Corporation is the technical staff's wide-ranging expertise and its ability to stay abreast of new technological developments and program support issues associated with rapidly evolving space systems. Contributing capabilities are provided by these individual organizations:

Electronics and Photonics Laboratory: Microelectronics, VLSI reliability, failure analysis, solid-state device physics, compound semiconductors, radiation effects, infrared and CCD detector devices, data storage and display technologies; lasers and electro-optics, solid state laser design, micro-optics, optical communications, and fiber optic sensors; atomic frequency standards, applied laser spectroscopy, laser chemistry, atmospheric propagation and beam control, LIDAR/LADAR remote sensing; solar cell and array testing and evaluation, battery electrochemistry, battery testing and evaluation.

Space Materials Laboratory: Evaluation and characterizations of new materials and processing techniques: metals, alloys, ceramics, polymers, thin films, and composites; development of advanced deposition processes; nondestructive evaluation, component failure analysis and reliability; structural mechanics, fracture mechanics, and stress corrosion; analysis and evaluation of materials at cryogenic and elevated temperatures; launch vehicle fluid mechanics, heat transfer and flight dynamics; aerothermodynamics; chemical and electric propulsion; environmental chemistry; combustion processes; space environment effects on materials, hardening and vulnerability assessment; contamination, thermal and structural control; lubrication and surface phenomena.

Space Science Application Laboratory: Magnetospheric, auroral and cosmic ray physics, wave-particle interactions, magnetospheric plasma waves; atmospheric and ionospheric physics, density and composition of the upper atmosphere, remote sensing using atmospheric radiation; solar physics, infrared astronomy, infrared signature analysis; infrared surveillance, imaging, remote sensing, and hyperspectral imaging; effects of solar activity, magnetic storms and nuclear explosions on the Earth's atmosphere, ionosphere and magnetosphere; effects of electromagnetic and particulate radiations on space systems; space instrumentation, design fabrication and test; environmental chemistry, trace detection; atmospheric chemical reactions, atmospheric optics, light scattering, state-specific chemical reactions and radiative signatures of missile plumes.

Center for Microtechnology: Microelectromechanical systems (MEMS) for space applications; assessment of microtechnology space applications; laser micromachining; laser-surface physical and chemical interactions; micropropulsion; micro- and nanosatellite mission analysis; intelligent microinstruments for monitoring space and launch system environments.

Office of Spectral Applications: Multispectral and hyperspectral sensor development; data analysis and algorithm development; applications of multispectral and hyperspectral imagery to defense, civil space, commercial, and environmental missions.